MXene-containing composite electrodes for hydrogen evolution: Material design aspects and approaches for electrode fabrication

Sergii A. Sergiienko [a],[*], Daniela V. Lopes [a], Gabriel Constantinescu [a], Marta C. Ferro [a], Nataliya D. Shchaerban [b], Obid B. Tursunov [c], Viacheslav I. Shkepu [d], Hanna Pazniak [e], Nataliya Yu. Tabachkova [f], Enrique Rodríguez Castellón [h], Jorge R. Frade [a], Andrei V. Kovalevsky [a]

[a] Department of Materials and Ceramics Engineering, CICECO − Aveiro Institute of Materials, University of Aveiro, 3810-193 Aveiro, Portugal
[b] L.V. Pisarzhevsky Institute of Physical Chemistry of NAS of Ukraine, 31 Nauki Ave., Kyiv, 03028, Ukraine
[c] Department of Power Supply and Renewable Energy Sources, Tashkent Institute of Irrigation and Agricultural Mechanisation Engineers, Qari Niyoziy 39, 100000 Tashkent, Uzbekistan
[d] Department of Chemistry, Faculty of Science, Masaryk University, Kamenice 5, 625 00 Brno, Czech Republic
[e] Institute PPRIME - UPR 3346 CNRS - Universite de Poitiers, France
[f] National University of Science and Technology MISiS, Leninskii pr. 4, Moscow 119049, Russia
[h] Department of Inorganic Chemistry, Faculty of Sciences, University of Malaga, 29071, Malaga, Spain

HIGHLIGHTS

- $Ti_3C_2Al_z$ (z > 1) MAX phases containing Al excess were synthesized.
- The composites based on Ni−Al alloy and $Ti_3C_2Al_z$ phase (z > 1) were obtained.
- Processing of MXene-containing electrodes under F-free conditions is demonstrated.
- Etching in alkaline medium forms active MXene- and Ni-containing surface layer.
- MXene- and Ni-containing electrodes show enhanced activity towards the HER.

ARTICLE INFO

ABSTRACT

This work explores the possibilities for the processing of Ni- and $Ti_3C_2T_x$ (T = OH, O) MXene-containing composite electrodes, by co-pressing and plastic deformation or by etching of the electrodes prepared directly by self-propagation high-temperature synthesis (SHS). Various material design approaches were also explored. In order to tune the Ti_3C_2 interlayer distance in Ti_3C_2Al MAX phase, an introduction of additional Al to form $Ti_3C_2Al_z$ materials with z > 1 was attempted. Self-propagation high-temperature synthesis of powder mixtures with extra Ni and Al content (e.g. Ni:Ti:Al:C = 1:2:3:1) resulted in SHS products containing $Ti_3C_2Al_z$ z > 1 material and Ni−Al alloys. Further etching of these products in 10M NaOH allowed the direct formation of electrodes with active surface containing $Ti_3C_2T_x$ (T = OH, O) MXene- and Raney nickel-containing composites. The electrochemical studies were focused on hydrogen evolution and showed the potential for boosting the electrochemical reaction in Ni and MXene-containing composite electrodes,

---

especially at high current densities. The guidelines for the processing of such electrodes under fluorine-free conditions are proposed and discussed.

Introduction

Ni-based electrodes are commonly used as cathodes in alkaline electrolysers for the production of hydrogen, provided by their low cost and corrosion resistance. MXenes are shown to be promising electrocatalysts either alone or as a part of the MXene-based materials [1]. As a support MXenes can modify the catalytic properties of metal nanoparticles [2]. For the effective use of MXenes as electro-catalysts and co-catalysts, several conditions must be met including: high electrical conductivity, low mass transfer limitations, sufficient stability and preferable use of active nonprecious catalysts components. A promising concept may be based on the use of well-established electrocatalytic material as a matrix with the incorporation of MXenes. Regarding the hydrogen evolution reaction (HER), Ni-based alloys and Ni-based hetero-structures exhibit the most promising electrocatalytic activity, partially owing to the possibility of fine-tuning of their surface adsorption properties by incorporated elements or domains [3].

In acidic conditions the electrocatalytic activity according to the so-called volcano plot for HER is controlled by the H adsorption free energy [4]. According to the recent studies [5,6], no pure element (except for a few noble metals) can efficiently act as a catalyst in the hydrogen evolution reaction. Hence, the only option to employ inexpensive compounds for HER electrocatalysis is to combine several elements or phases with weak and strong bonds with hydrogen. In this case, two types of hydride bonds can be formed, including a strong one to support the H adsorption process and a weak one to facilitate the H_2 formation. It is generally believed that the H adsorption is initiated on the element (composition) having a strong bond with hydrogen, and the adsorbed H can move via surface diffusion. The weak bond of the element (composition) with hydrogen should break down easily leading to the formation of an H_2 molecule.

Several research works have convincingly shown that the MXenes with −OH terminations or with oxygen terminations e.g. $Ti_3C_2O_2$, Ti_2CO_2, Nb_2CO_2 could be used as efficient noble metal-free catalysts [4,7]. After etching in HF solution, the MXenes predominantly exist in the form of Ti_2CT_x or $Ti_3C_2T_x$ (where T_x are −OH and −F terminations), but in such state their electrocatalytic activity is low [8]. A treatment in alkaline media promotes the formation of −OH terminations and boosts the electrocatalytic activity.

Thus, a promising electrocatalytic platform for HER may comprise metallic Ni having a relatively strong bond with hydrogen (negative Gibbs free energy of hydrogen adsorption, ΔG_H) [9] and MXenes (terminated with oxygen) e. g Nb_2CO_2 or Mo_2CO_2 that have slightly positive ΔG_H or Ti_2CO_2 that have close to optimal ΔG_H [4,10].

In alkaline medium, the complex process of HER suffers from slow reaction kinetics due to the additional water dissociation step. Therefore, the electrocatalysts with suitable performance in acidic media usually lose catalytic activity in alkaline media [11,12]. MXenes are therefore of interest as a part of complex catalysts for hydrogen evolution in alkaline medium, particularly due to the exothermic water adsorption resulting in its easier dissociation [13].

Mass transfer limitations also affect HER processes. Usually, in 2D materials (e.g. MoS_2) only the edge sites are active toward HER, while in MXenes basal plane is catalytically active toward HER [8]. Therefore, the surface accessibility improvement in MXenes by increasing the interlayer distance through the intercalation of various molecules with subsequent delamination and exfoliation by ultrasonic treatment is usually used [14]. This process can destroy MXene layers and connections between these layers and particles, increasing the electrical resistance. Thus, the formation of $Ti_3C_2Al_z$ materials with $z > 1$ and further MXene structure with increased distance between the layers can reduce the diffusion limitation and, therefore, enhance the catalytic performance.

A significant obstacle towards the application of MXenes is represented by the necessity to involve hazardous and toxic HF etching during synthesis. Etching MAX phases using alkaline media (e.g. 10M NaOH) instead is a very attractive way to obtain such materials and can greatly simplify the introduction of those materials in industry [15]. Also, the presence of −F terminations on the basal planes of Ti-based MXenes is detrimental to the HER, therefore to avoid −F and to increase −OH terminations alkaline treatment can be applied [8,16].

This work intends to compare both etching procedures in terms of relevant effects on HER processes in composite MXene-containing electrodes. Material design approaches involved classical MXenes obtained from Ti_3AlC_2 MAX phase, where the amount of Al was varied to tune the interlayer distance, and those derived from novel $Ti_3C_2Al_z$ ($z > 1$) and Ni-containing composites, to explore possible effects provided by the formation of Ni−Al alloys and to benefit from simultaneous etching and Raney nickel formation in alkaline conditions.

Material and methods

Synthesis and preparation of materials

Samples were synthesized from commercially available powders of titanium (Alfa Aesar, 10,386, −325 mesh, less than 45 μm, 99%), carbon black, acetylene (Alfa Aesar, 39,724, 50% compressed, 99.9+%), aluminium (Alfa Aesar, 11,067, −325 mesh, less than 45 μm, 99.5%) and nickel (Alfa Aesar,

10,256, APS 3—7 μm, 99.9%). The starting powders were sequentially mixed and pressed to break up the particle agglomerates, followed by ball milling for 2 h with ethanol for obtaining a suitable homogeneous mixture. Next, the powder mixtures were pressed uniaxially in the shape of discs (diameter = 25 mm, thickness approx. 3—4 mm). The sintering of the powder compacts was performed by self-propagation high-temperature synthesis (SHS). Initial compositions, corresponding denominations and processing parameters of the samples are listed in Table 1.

Post-processing of the powders

After the synthesis, the SHS products were ground to decrease the average particle size down to about 0.1 mm. Etching of Al to form MXenes from the milled SHS products was carried out in a polypropylene jar with external water cooling. In the case of etching in HF solution (45 wt% water), the acid was added by small portions to the aqueous suspension (20—30 wt% in water) of the SHS products. Molar Al:HF ratio in most cases was equal to 1:6, considering the total amount of Al in the starting mixture. During etching, the suspensions were continuously stirred for 48 h using a magnetic stirrer. As a next step, the obtained powders were washed several times with distilled water (at room temperature) and filtered using vacuum filtration with a conventional filter paper. Samples were posteriorly washed with ethanol to remove the residual water. Then, the MXene-containing suspension was filtered on a vacuum filter and dried at room temperature.

In order to perform etching in alkaline conditions, an excess of 10 M NaOH solution was used, e.g. 4 g of SHS products and 50 mL of 10 M NaOH solution. The suspension was filtered under vacuum, washed with distilled water several times and dried at room temperature.

Preparation of electrodes

For convenience, different working electrode designs are further denoted as type 1—3. The type 1 composite electrodes were processed by pressing MXene powder 14m (0.4 g) with 3.6 g of Ni powder to form discs with a diameter of 25 mm and ~2 mm thick (Fig. S1A).

The type 2 electrode was prepared by pressing 3 g of Ni powder and 1 g of MAX phase powder sample 14a, followed by sintering (T = 800 °C, 1 h) and etching during 24 h in 10 mL 5 % wt. HF solution to obtain Ni/MXene composite (Figs. S2A and B).

The type 3 electrodes were produced directly by SHS (Fig. S3A). The initial mixture of powders (4 g) was compacted in a cylindrical mold (25 mm of diameter) at about 3.5 MPa to produce ~3 mm thick samples. To initiate the SHS process, a small propane oxygen burner was used. To avoid oxidation of the samples during SHS process in air, they were covered with carbon black. The $Ti_3C_2T_x$ MXene/nano-Ni composite layer on the surface of Ni—Al/MAX phase electrodes was formed by etching in 1) 5 wt % HF solution, or in 2) 10M NaOH solution. In the first case, the etching of the electrodes was performed by immersing in 30 mL of 5 wt % HF solution, during 24 h at room temperature, followed by washing electrodes in distilled water. In the second case, the electrodes were immersed in 30 mL of 10M NaOH solution during 1—5 days, followed by washing in distilled water. Images of electrodes after etching are presented in Figs. S3A and F (sample 61p electrode), or Fig. S3B (sample 60s electrode).

Material characterization

The phase composition was assessed by X-ray diffraction analysis (XRD), using a Rigaku D/Max-B diffractometer system (CuKα radiation, 0.154056 nm). Hitachi SU-70 scanning electron microscopy (SEM) combined with energy dispersive spectroscopy (EDS) analysis (Bruker Quantax 400 detector) was used to characterize the relevant microstructural features. TEM imaging was performed on a JEOL 2200FS TEM (200 kV Schottky field emission). X-Ray Photoelectron spectroscopy (XPS) measurements were carried out using a Physical Electronics PHI 5700 spectrometer with non-monochromatic Mg Kα radiation (300 W, 15 kV, 1253.6 eV) with a multi-channel detector. Spectra were recorded in constant pass energy mode at 29.35 eV using a 720 μm diameter analysis area. Binding energy (BE) values were referenced to the C1s peak (284.8 eV) from the adventitious contamination layer. The PHI ACCESS ESCA-V6.0 F software package and Multipak v8.2b were used for acquisition and data analysis, respectively. A Shirley-type background was subtracted from the signals. Recorded spectra were fitted using Gauss-Lorentz curves to determine the binding energy of the different element core levels more accurately. The error in BE was estimated to be ca. 0.1 eV. Samples were also studied after etching with an Ar^+ gun (4 kV, 2×2 mm^2) for 6 min.

Electrochemical measurements

Electrochemical measurements were carried out using Autolab potentiostat (PGSTAT 302) connected to the electrochemical three-electrode cell. A Pt wire was used as a counter electrode (CE) and Hg|HgO|NaOH (1M) (+0.098 V versus saturated hydrogen electrode) as a reference electrode connected by a Luggin capillary to the electrolyte as previously described in Ref. [17]. All experiments were performed at room temperature with NaOH (1 M) as an electrolyte. Each working electrode tested was composed of ~4 g of material and had 25 mm in diameter, and about 3 mm of thickness. Hydrogen evolution tests were performed between 0 and -1.5 V with a scanning rate of 1 mV/s. The current density values were calculated from the geometric area of each electrode (~10 cm^2). To estimate the electrocatalysts surface area, the capacitance method was chosen [18]. The electrochemical surface area (ECSA) was calculated from the cyclic voltammetry data around the open circuit potential (OCP), using different scan rates from 10 to 120 mVs^{-1}. For this, the values of double-layer capacitance (Cdl) were extracted from the CV curves. The Cdl values for the samples were estimated by plotting the $\Delta J = (|Ja| - |Jc|)/2$ (at overpotential in the middle of the cycling range) against the CV scan rate, Ja and Jc current density of anode and cathode, respectively. The slope value is equal to the Cdl and it can be used to represent the ECSA [19]. The ECSA values were represented per unit of surface area (areal capacitances, F/cm^2), due to difficulty in determining the mass of the etched layer. This seems to be a suitable

Table 1 – Denominations and initial composition of the samples, processing and etching conditions, and electrochemical surface area of the corresponding electrodes.

Samples (powders and electrodes)	Initial composition in SHS, Ni:Ti:Al:C, molar ratios				Ball milling time, hours	Etching conditions, HF, molar ratio Al: HF, or 10M NaOH, temperature, time days	ECSA, (cm²$_{ECSA}$ per cm²$_{geo}$) at 10–60, 60-120 mVs⁻¹
	Ni	Ti	Al	C			
13a	0	2	1.2	1	2		
13m	0	2	1.2	1	2	HF, 1 : 6	
33a	0	2	1.5	1	2		
33a electrode	0	2	1.5	1	2		
33b electrode	0	2	1.5	1	2	HF, 1 : 1	
14a	0	2	2	1	2		
14m	0	2	2	1	2	HF, 1 : 6	
61a	0	2	3	1	2		
61a electrode	0	2	3	1	2		
61b electrode	0	2	3	1	2	HF, 1 : 1	
61d	0	2	3	1	2	HF, 1 : 2	
61m	0	2	3	1	2	HF, 1 : 6	
61k	0	2	3	1	2	HF, 1 : 6	
61t electrode	0	2	3	1	2	10M NaOH, 20 °C, 2 days	
61p electrode	0	2	3	1	2	10M NaOH, 70 °C, 2 days	320, 50
62a electrode	0	2	3.5	1	6	10M NaOH, 50 °C, 2 days	350, 150
62p electrode	0	2	4	1	6	10M NaOH, 20 °C, destroyed	
Ni	1	–	–	–			
36a	0.2	2	1.5	1	2		
38a	0.4	2	1.5	1	2		
37a	0.4	2	2	1	2		
37d	0.4	2	2	1	2	HF, 1 : 2	
37r	0.4	2	2	1	2	HF, 1 : 3	
37f	0.4	2	2	1	2	HF, 1 : 4	
37x	0.4	2	2	1	2	10M NaOH, 20 °C, 1 day	
37z	0.4	2	2	1	2	10M NaOH, 20 °C, 2 days	
37y	0.4	2	2	1	2	10M NaOH, 20 °C, 3 days	
53a	1	2	1	1	2		
54a	2	2	1	1	2		
60a	1	2	3	1	2		
60a electrode	1	2	3	1	2		
60d	1	2	3	1	2	HF, 1 : 2	
60m	1	2	3	1	2	HF, 1 : 4.5	
60b electrode	1	2	3	1	2	HF, 1 : 1	
60c	1	2	3	1	2	10M NaOH, 20 °C, 1 day	
60t electrode	1	2	3	1	2	10M NaOH, 20 °C, 2 days	
60p electrode	1	2	3	1	2	10M NaOH, 70 °C, 2 days	
60s electrode	1	2	3	1	2	10M NaOH, 70 °C, 5 days	400, 100
60n electrode	1	2	3	1	2	10M NaOH, 160 °C, 2 days	
60x electrode	1	2	4	1	6	10M NaOH, 70 °C, 5 days	460, 120
63a electrode	1	2	5	1	6	10M NaOH, 20 °C, destroyed	
70a	2	2	4.5	1			
100a	2	0	3	1			

approximation because the specific capacitance measured also includes the pseudocapacitance in addition to electrical double-layer capacitance. The specific capacitance values for a flat standard with 1 cm² of the real surface area is generally in the range of 20–60 μFcm⁻² (40 μF cm⁻² was taken as the average value) [8]. Also, to evaluate areal capacitances of the obtained materials which can be used in supercapacitor applications, wide cyclic voltammetry cycles were recorded using different scan rates in the range from −0.4 to −0.9 V [20,21]. The areal capacitance was calculated by current integration over time [22]. The electrochemical impedance spectroscopy (EIS) was carried out using the same potentiostat at open circuit potential, with a 10 mV of amplitude and frequencies ranging from 100 KHz to 10 mHz [23].

Results and discussions

The influence of Al content in the initial precursors on the structure of resultant SHS products

Using an excess of aluminium as compared to titanium is expected not only to tune the Ti_3C_2 interlayer distance in Ti_3C_2Al, but also to facilitate the formation of the desired MAX phase [24]. Fig. 1A demonstrates the XRD data of SHS products obtained with different amount of Al in the initial compositions, from Ti:Al:C = 2:1.2:1 to 2:4:1. A slight shift and broadening of the XRD peaks related to the Ti_3AlC_2 MAX phase towards smaller angles on increasing the Al content in the

initial mixture can be observed (Fig. 1B). This lattice expansion is likely linked to the incorporation of additional Al atoms between the Ti_3C_2 layers. The SHS products also contain intermediate phases such as $TiAl_3$ and TiC.

The SHS products typically possess a so-called "core shell structure" [25], with the core rich in carbon. The etching in HF is expected to proceed faster for the product with a higher Al content, followed by the removal of Al from ternary carbide and formation of MXene. After HF etching of the SHS products with a higher nominal amount of Al, a shift in the MXene XRD small-angle diffraction peak is observed (Fig. 2A). Namely, the position of the first small-angle diffraction peak shifts from 2θ of 8.9 to 5.7° on increasing the amount of Al from Ti:Al:C = 2:1.2:1 (sample 13m) to 2:3:1 (samples 61d). Similar shifts of the discussed peak were observed in other publications (e.g., from 9 to 6.5° [26], from 8 to 4.5° [14]), promoted by the intercalation of MXene with various organic compounds and delamination under ultrasonic conditions. Partial etching of the SHS products with high Al content, when only 50% of the HF required for Al dissolution is used, expectedly results in coexistence of the MXene and residual Ti_3AlC_2 MAX phase with typical Al content (sample 61d, Fig. 2A). Adding a small excess of HF (Fig. 2A, sample 61k) leads to progressive MXene

formation and appearance of the peaks corresponding to AlF_3. The part of AlF_3 apparently remains between Ti_3C_2 layers and, similarly to the intercalation of organic compounds, mentioned above, results in a significant shift of the small-angle diffraction peak towards even lower angle. Further washing and dissolution of AlF_3 is accompanied with the structure contraction and smaller distance between MXene sheets (Fig. 2A, sample 61m).

Usually, the distance between the centers of MXene sheets (c-lattice parameter) is about 1 nm, while the thickness of one Ti_3C_2 layer also is close to 0.98 nm [27,28]. In the MXene obtained here from the Al-rich SHS products, c-lattice parameter corresponds to 1.55 nm (calculated from the position of small-angle diffraction peak at 5.7° for sample 61d, Fig. 2A). Therefore, the average interlayer spacing between the MXene sheets should be equals to 0.55 nm. In fact, the results of TEM inspection of the sample 61d after etching (Fig. 2B) shows that the distance between the layers can be even larger. Also, some disordering of the structure is observed. Assuming the size of the water molecule equal to 0.28 nm, the mentioned distance between the MXene layers is sufficient for water diffusion in the space between the layers, essential for electrocatalytic boosting.
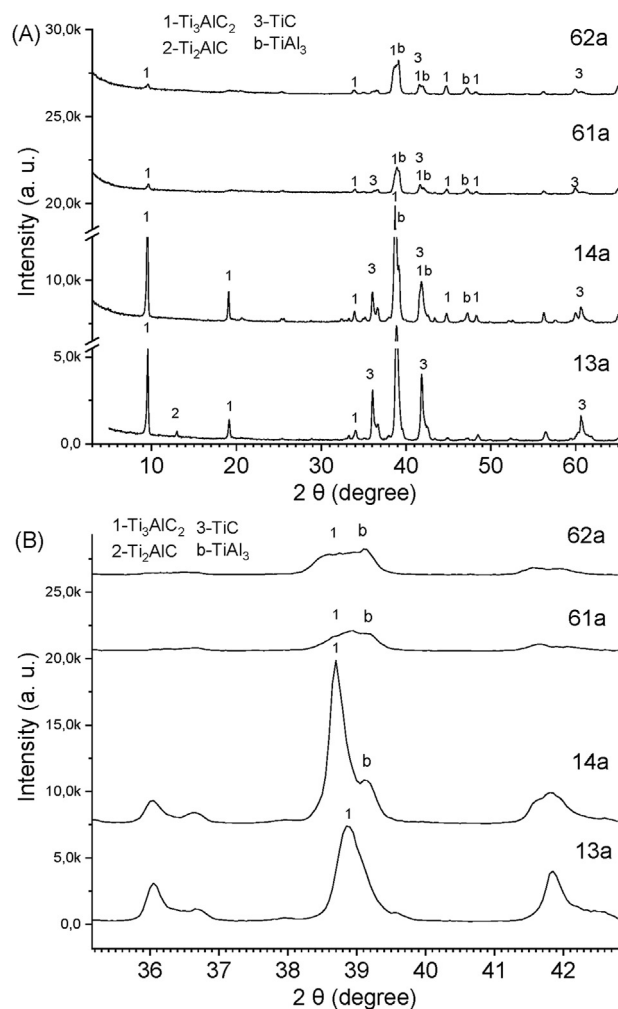

Fig. 1 – The influence of Al content in initial precursor on the structure of resultant SHS products (A, B).
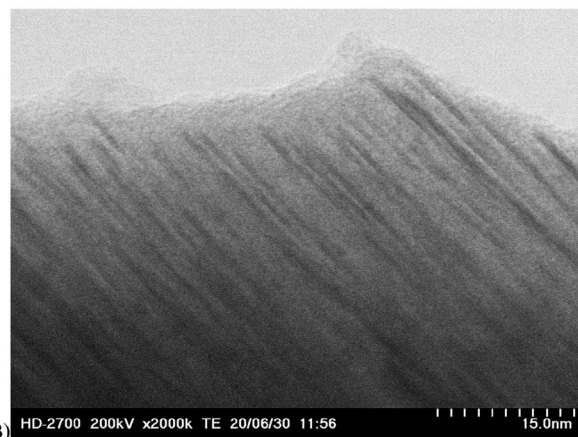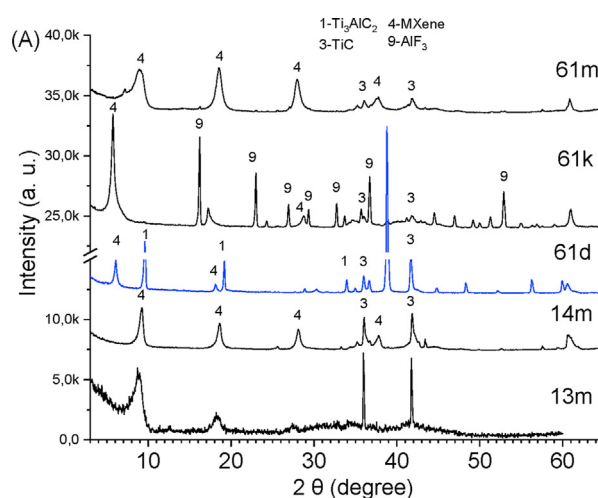

Fig. 2 – The influence of Al content in initial precursor on the structure of resultant MXene-containing products (A). TEM image of the particles from sample 61d (B).

As it is generally accepted, the carbon particle size has the strongest effect on the structure of the reaction products in such systems [29]. The XRD data for the samples after etching suggests that a considerable amount of carbon remains in carbon-rich "cores" corresponding to the conventional Ti_3C_2Al phase. In order to increase the homogeneity of the SHS products and to reduce "core" size in such "core-shell structure" ball milling of the initial powder mixture was performed during 6 h in the case of samples with high Al content (62a and 62p). Ball milling makes it possible to reduce particles size of the initial powders, thus increasing the reaction rate and the temperature during SHS process. This, in turn, results in decreasing of the content of the initial unreacted components (Al, C) and intermediate products (TiC, $TiAl_3$, Ti_3C_2Al), while promoting the formation of the target product ($Ti_3C_2Al_z$, z > 1).

Ni—Al/MAX phase and nano-Ni/$Ti_3C_2T_x$ MXene materials

While searching for the appropriate electrode structures, several preparation methods of nickel-containing MXene materials were attempted. One of the disadvantages of the type 1 electrode is a weak connection between the particles leading to the disintegration of the electrode, further promoted by the hydrogen evolution. On the contrary, the preparation method of type 2 electrode forming MXene particles incorporated in the Ni electrode matrix. Despite the use of relatively coarse 3-7-micron-size Ni powder, the plasticity of the metal particles during pressing facilitates the formation of good contacts between the phases and reliable electrode structure.

In many cases, when the catalyst is presented by the combination of several phases or particles, the reaction rate scales with perimeter length rather than with an area of contact between these phases [30]. Therefore, the formation of nanostructured Ni-containing MXene structure directly at the electrode surface is of great interest. Taking into account the above strategies, the type 3 electrodes were prepared directly by SHS of pressed powders mixtures with different Ni:Ti:Al:C ratios. This method, in comparison to the others, does not include stages like MAX phase crushing and sintering. As known, Ni apparently does not form MAX phases, and according to previous works, small amounts of Ni additives can suppress the grain growth and decompose Ti_3AlC_2 during sintering with subsequent formation of Ni-based compounds [31].

To investigate the possible formation of Ni-containing MAX phase materials with different ratio between components, several samples were prepared. Increasing Al ratio in the initial mixture from 1.5 (sample 36a) to 2 (sample 37a) allows one to obtain SHS products (composites) consisting of Ti_3AlC_2 MAX phase together with Ni_xAl_y compounds and low TiC content (Fig. 3A). Lack of Al in the initial mixture (sample 38a) leads to the appearance of the additional peaks in XRD diffractogram related to $Ti_xNi_yAl_z$ compounds, e.g. $TiNi_2Al$.

When a higher Ni content is combined with a low Al amount (samples 53a or 54a), the predominant formation of $Ti_xNi_yAl_z$ compounds, Ni_2Al_3 and TiC is observed (Fig. 3B). Adding Al into the reaction mixture allows one to obtain reaction products containing predominantly Ti_3AlC_2 MAX phase and Ni_2Al_3 with lower contents of TiC and $Ti_xNi_yAl_z$ compounds (sample 60a, Fig. 3B). At high Al content in the initial

reaction mixture (sample 63a), the reaction temperature decreases and a significant number of unreacted components are present in the SHS products. Also, further increase of the content of Ni and Al in the initial reaction mixture (sample 70a, XRD pattern Fig. S4) leads to a significant decrease in MAX phase content in the SHS products. Simultaneously, an increased amount of titanium carbide is observed.

Partial etching of Ni_2Al_3, Ti_3AlC_2 and $Ti_3C_2Al_z$ (z > 1) containing SHS products in 5 wt % HF solution leads to a decrease in Ni_2Al_3 amount and appearance of the peaks related to MXene (sample 60d Fig. 4, and sample 37d Fig. S5A). It should be noted, that after etching in HF solution and washing in water, the small-angle diffraction peak remains in the same position (5.8° 2θ angles) and the structure does not compress after drying (sample 60m Fig. 4, and samples 37r, 37f, Fig. S5A), in opposite to the case of the sample without nickel (sample 61m, Fig. 2A).

Partial etching of the sample 37a in 10M NaOH solution (samples 37x, 37z, samples 37y, Fig. S5B) leads to the dissolution of Al-rich layer of SHS products, but the peaks related to Ni—Al alloy become more intense (samples 37x) than in the case of etching in HF solution. This is likely due to the fact that Ni dissolution from Ni containing SHS products in the case of
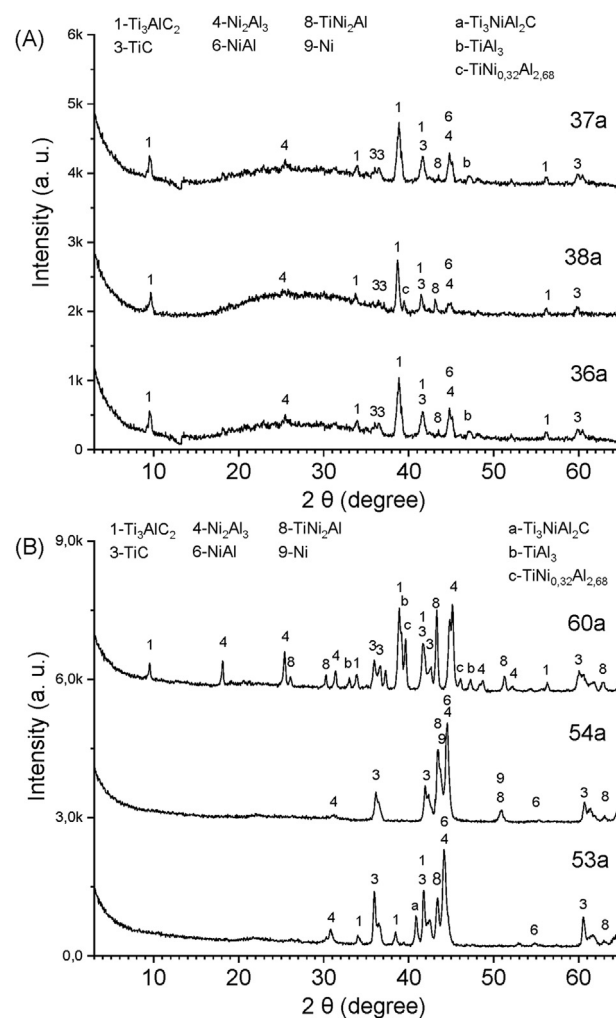

Fig. 3 — The influence of Ni addition to the initial precursor on the structure of resultant SHS products (A, B).
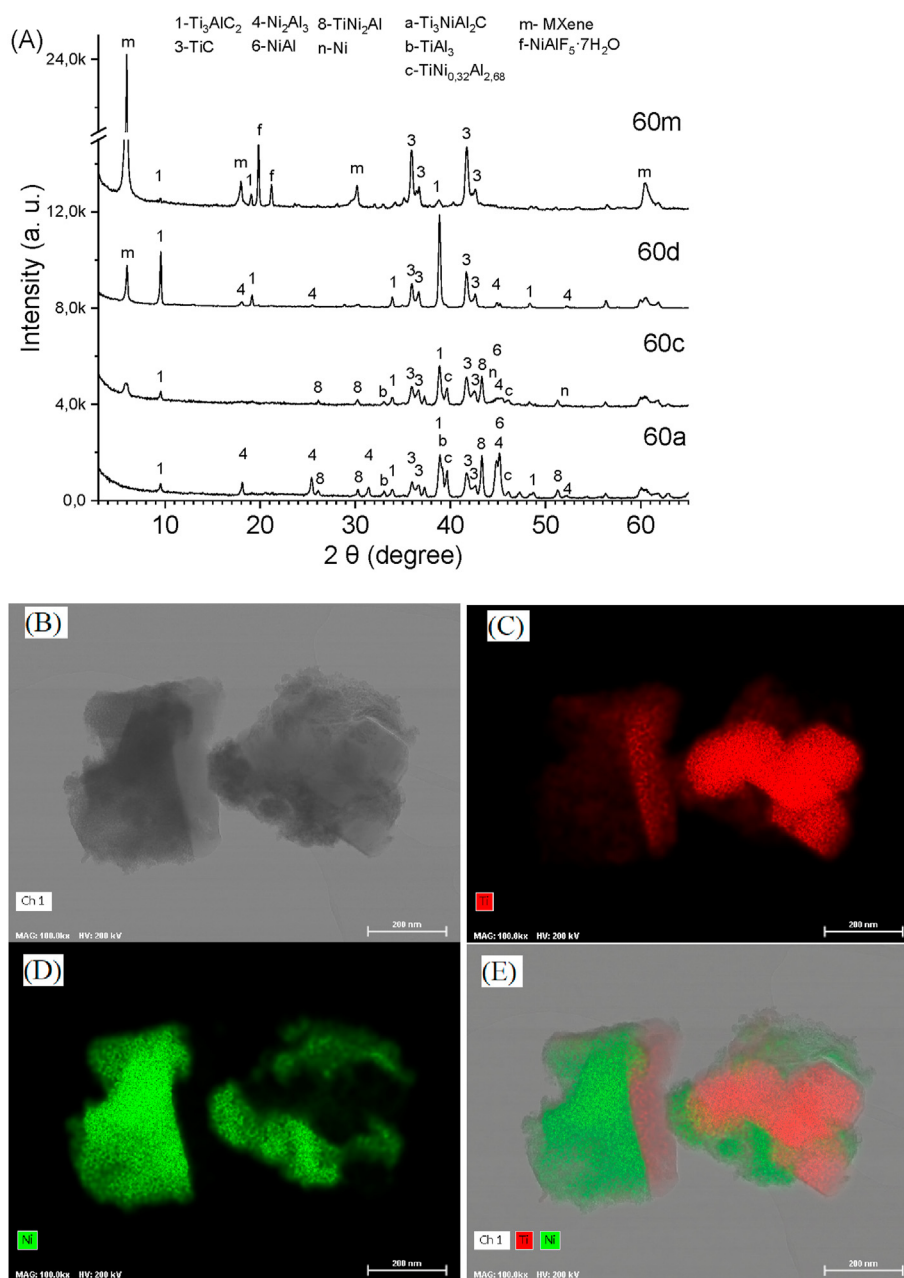
Fig. 4 – XRD patterns of the samples obtained by etching of Ni-containing SHS products in 5% HF (60d, 60m) or 10M NaOH (60c) solutions (A). TEM image (B) and TEM/EDS mapping (C, D, E) of the sample 60c, showing the distribution of Ti (red color) and Ni (green color).

etching in HF solution occurs together with Al. Etching of sample 37a in 10M NaOH solution during 2 days (sample 37z), and during 3 days (sample 37y) leads to further suppression of the XRD peaks related to Ni–Al alloys in SHS products.

In the case of sample 60a with higher Ni and Al content, the appearance of small-angle diffraction peak (6.0°, 2θ angles) was observed not only when Al etching was conducted in the HF solution (60d, 60m, Fig. 4A), but also after etching in 10 M NaOH solution at room temperature (60c, Fig. 4A). The appearance of these small-angle diffraction peaks is accompanied by the vanishing of the peaks corresponding to Ni–Al alloys. Also, the presence of small peaks, probably related to nanostructured Ni, was observed. As known, the dissolution

of Al from metal-Al alloys (dealloying [32]), e.g. Ni–Al alloys in 10M NaOH leads to formation of nanostructured Ni Raney [33] known for excellent electrocatalytic activity. TEM/EDS mapping demonstrates the distribution of nanostructured Ni on the surface of Ti_3C_2 layers (sample 60c) after etching in 10M NaOH (Fig. 4B–E).

X-ray photoelectron spectroscopy analysis

XPS characterization of several representative materials, including non-etched 60a, HF-etched 61k and NaOH-etched 60s samples (Table 1), was undertaken to understand the surface chemistry and relevant impacts of the etching

procedures. Both Ar+-sputtered and "as-prepared" samples were analyzed, corresponding full spectra are shown in Figs. S9, S10, S11. The work [34] underlines the importance of such an approach for the materials containing sensitive surface species, although non-sputtered samples usually present a large number of contaminations coming from the ambient atmosphere and specific processing procedures.

General XPS spectra of the sample 61k in the F 1s region (Fig. S9) show the presence of F-terminated Ti, which is typical for MXenes obtained by etching in fluorine ion-containing media [16]. Corresponding peaks in this region are absent in the spectra of the sample 60s, processed by etching in 10M NaOH (Fig. S10).

The Ti 2p signal for the sample 61k shows the presence of at least two types of Ti (Fig. 5A, Table S1), Ti 2$p_{3/2}$ at 454.7 eV (62%) related to Ti carbide photoemission and arises from Ti$_3$C$_2$ [16,34], and Ti (Ti 2$p_{3/2}$ 458.5 eV (38%)) is probably related to oxide. After Ar$^+$ treatment the presence of one type of Ti is observed at 455.1 eV assigned to Ti carbide.

The Ti 2p signal for the sample 60a (with Ni, non-etched) again shows the presence of at least two types of Ti (Fig. 5C, Table S1), Ti forming part of a carbide (Ti 2$p_{3/2}$ at 453.6 eV (50%)) and Ti(IV) (Ti 2$p_{3/2}$ 458.3 eV (50%)) probably as oxide. After Ar$^+$ etching, the presence of only one type of Ti observed at 454.3 eV and assigned to Ti carbide.

The Ti 2p signal for the sample 60s (with Ni, after etching in 10M NaOH) shows the presence of significant amount of oxidized Ti (IV) (Ti 2$p_{3/2}$ 458.2 eV (90%)) and also Ti forming part of a carbide (Ti 2$p_{3/2}$ at 454.6 eV (10%)) related to Ti$_3$C$_2$ of MXene (Fig. 5F, Table S1). After Ar$^+$ etching the ratio of Ti

carbide photoemission at 455.4 eV (54%) assigned to Ti^{2+} [34] becomes higher as compared to Ti (IV) oxide at 459.5 eV (46%). Similar spectra change also were observed [16] due to MXene partial oxidation after alkaline treatment. In general, oxygen content in sample 60s is higher compared to sample 61k due to absence of fluorine terminations and higher etching temperature (Table S2), with expected positive impact on the electrochemical activity.

The C 1s core level spectrum for the sample 61k (Fig. 5B, Table S1) of the fresh sample confirms the presence of carbide, detected at 281.2 and 282.1 eV. The presence of carbonate species at 288.5 eV (7%) is also observed. After Ar$^+$ etching, the carbonate is totally removed and two contributions due to carbide groups probably related to Ti$_3$C$_2$ at 282.0 eV (71%) and 283.2 eV (13%) are observed. In this case, the strong contribution of adventitious carbon is almost eliminated.

The C 1s signal for the sample 60a (Fig. 5D, Table S1) shows the presence of carbon in different forms, the weak presence of carbide is detected at 280.7 eV, the presence carbonate at 289.0 eV is also observed. After Ar$^+$ etching, carbonate is totally removed and two contributions with a high relative intensity due to carbide groups at 282.0 eV (63%) and 283.4 eV (16%) are clearly visible.

The C 1s signal for the sample 60s (Fig. 5G, Table S1) shows a high C content, which is reduced after Ar$^+$ treatment. The presence of carbide arising from Ti$_3$C$_2$ is detected at 281.3 eV (10%). The contribution at 284.6 eV can be assigned to C—C [34], occurring probably due to the presence of unreacted carbon after SHS process in samples with relatively high Ni content.
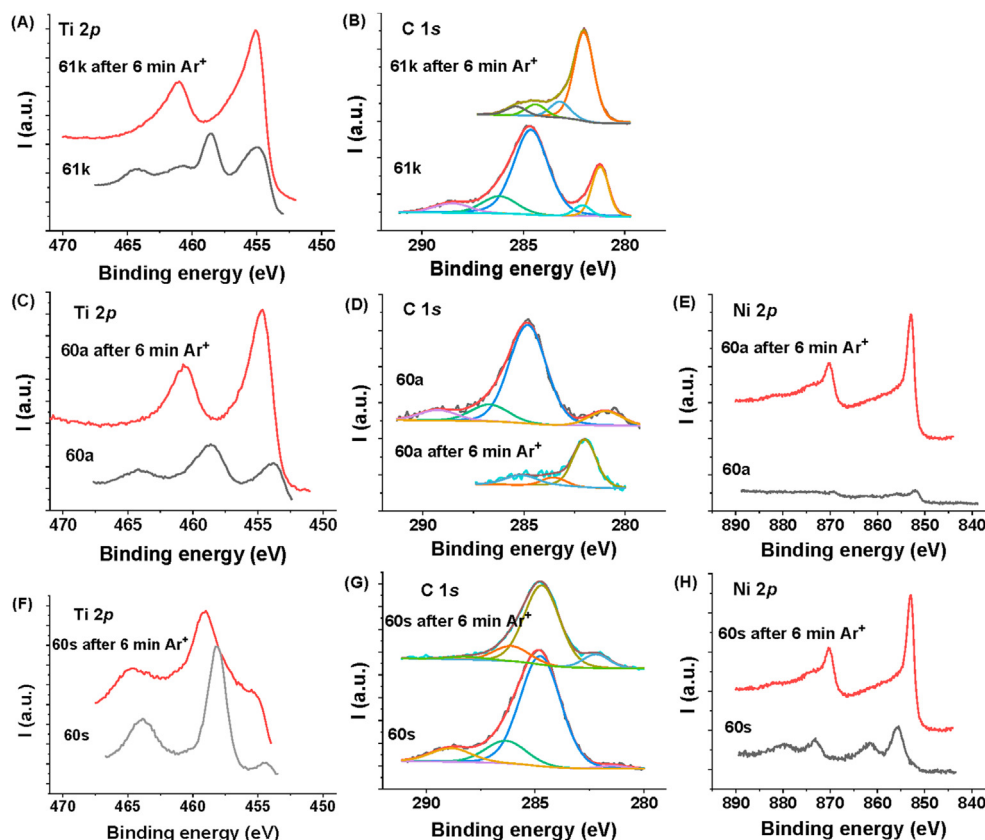

Fig. 5 — **XPS spectra in different regions obtained for the samples 61k (A, B), 60a (C, D, E) and 60s electrode (F, G, H).**

A weak Ni 2p signal is observed in the sample 60a (Fig. 5E, Table S1) with a main Ni $2p_{3/2}$ peak at 852.2 eV, a typical value for metallic Ni. After Ar^+ treatment, the Ni 2p is more clear and the main Ni $2p_{3/2}$ peak is shifted to 853.3 eV, probably corresponding to Ni_2Al_3.

In the sample 60s, a Ni 2p signal is observed with a main Ni $2p_{3/2}$ peak at 855.5 eV, a typical value for Ni(II) (Fig. 5H, Table S1. After Ar^+ treatment, the Ni 2p is modified and the main Ni $2p_{3/2}$ peak is shifted to 852.9 eV, indicating that the Ni(II) was reduced to Ni(0).

In general, the chemical environments derived from the XPS data corroborate the previous guidelines obtained from the XRD results. However, the inherent complexity and composite nature of the materials complicate a comparative analysis of the samples, representing a good challenge for future work.

Electrode surface morphology and structure

SEM studies coupled with EDS spectroscopy, performed for the materials under study, reveal the structures with complex morphology. SEM images of fractured type 3 electrode (61p) after etching in 10M NaOH during 2 days are shown in (Fig. 6). The central part of such electrode is represented by porous
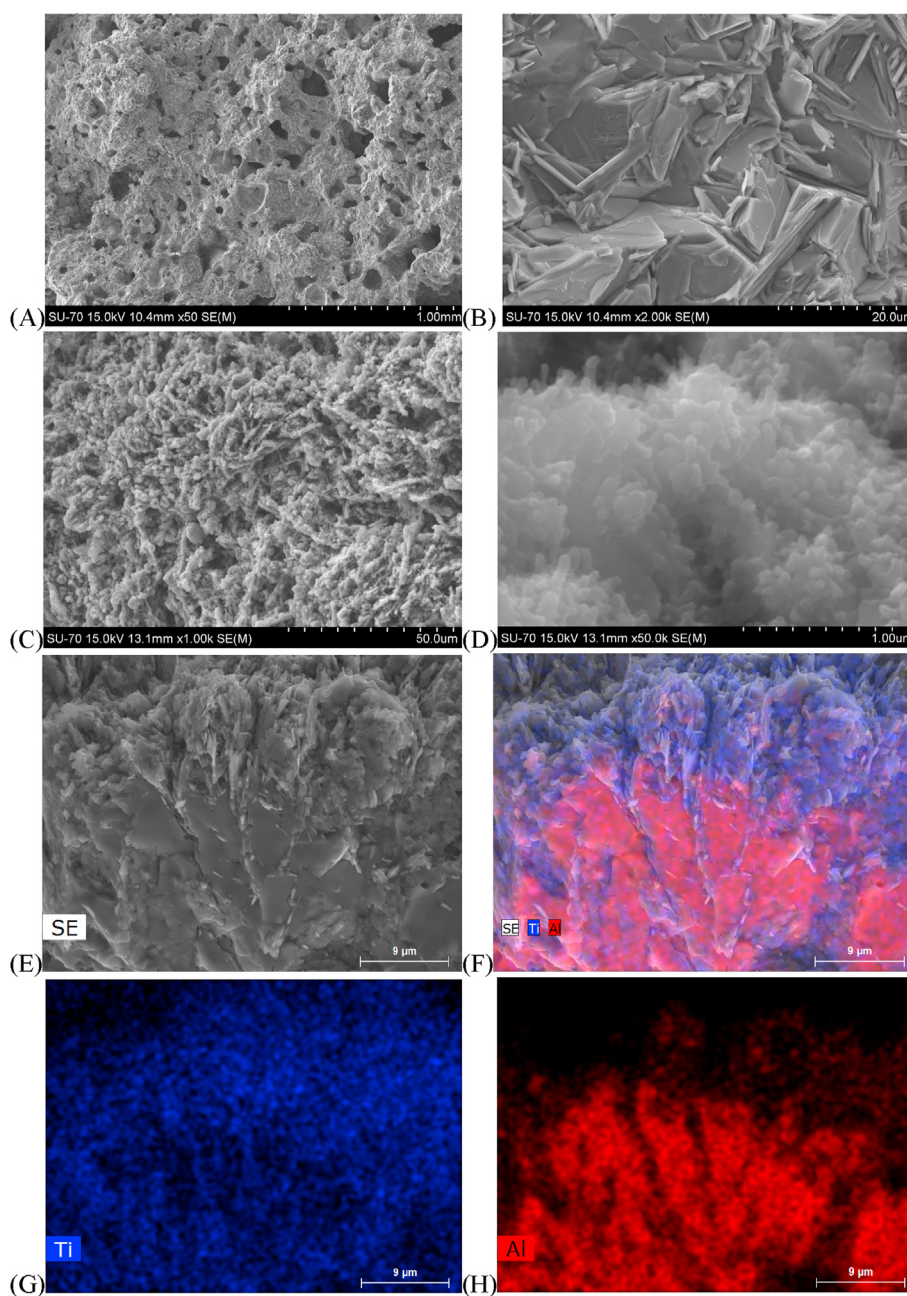

Fig. 6 – SEM images of the type 3 electrode (61p electrode): inner bulk, not etched part (A, B), surface of the electrode after etching (C, D). SEM/EDS mapping of the interface between etched and not etched parts of the electrode, showing the distribution of Al (red color) and Ti (blue color) in the surface layer (E, F, G, H).

products of SHS synthesis (Fig. 6A). Despite the apparently porous structure, the inner part of the electrode was mostly not exposed to the alkali solution, indicating that a significant amount of such macropores is closed. At higher magnification, the crystals of MAX phase in such SHS products become visible (Fig. 6B). The surface of such electrode after etching becomes more porous due to the dissolution of Al (Fig. 6C, D). The thickness of the etched layer reaches several microns, as confirmed by SEM/EDS mapping (Fig. 6E–H). The outer part of the layer exposed to NaOH is rich in titanium, while Al is mostly dissolved. This part also appears more nanostructured (Fig. 6D) and likely includes MXene particles. The inner part contains both Al and titanium (Fig. 6F, G, H, Figs. S6A, B, C, D) and corresponds to non-etched SHS products, mostly $Ti_3C_2Al_z$ (z > 1) and conventional MAX phase.

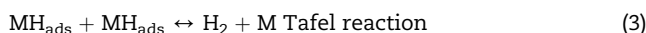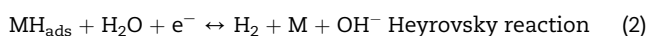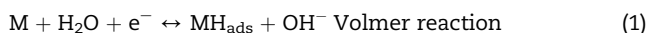### Hydrogen evolution and electrochemical measurements

Type 1 electrode shows approximately the same onset potential of hydrogen evolution (Fig. S1B) with Ni electrode (−0.94 V), while in the case of type 2 electrode the onset potential is slightly delayed (Fig. S2C). The disadvantages of such electrodes include relatively low area and perimeter of contact between the individual phases (Ni and MXene) which are represented mainly by micron particles. As a result, the co-catalytic effect is expected to be less pronounced as compared to the sintered nanostructured materials (type 3 electrodes). At the same time, more emphasis was given to type 3 electrodes, provided by the possibility to form catalytically active layers directly by etching of the Ni—Al alloy and MAX phase containing electrode followed by the formation of a nanostructured Ni and MXene containing composite layer attached to the electrode surface without any intermediate steps.

As can be seen from (Fig. 7A), the electrodes with higher Al content in SHS products (61a electrode) demonstrate lower overpotential of H_2 evolution compared to sample with low Al content (33a electrode). Etching of such electrodes (33a electrode, 61a electrode) in 5 wt% HF leads to decreasing overpotential of H_2 evolution, likely due to the formation of MXene layers at the electrode surface (33b electrode, 61b electrode). The electrocatalytic activity of sample 61b electrode is higher when compared to 33b electrode probably due to the greater

distance between $Ti_3C_2T_x$ layers and, therefore, a better access of the electrolyte to the catalytically active surface.

Moreover, further lowering of the onset overpotential of HER occurs (61p electrode, Fig. 7A), when 10 M NaOH is used for etching the electrode surface with higher Al content in SHS products (Ti:Al:C = 2:3:1) instead of the 5 wt% HF solution. The increase in catalytic activity is probably associated with the absence of fluorine groups (−F), while the T_x terminations in $Ti_3C_2T_x$ are hydroxyl groups (−OH) [8]. Further increase of Al content in such materials (62a and 62p electrodes, Table 1) makes it possible to reduce the etching temperature and slightly increase the catalytic activity, but such electrodes experience a rapid degradation.

The determination of the reaction mechanism of HER and the rate-determining step (RDS) can be performed using Tafel analysis. It is generally accepted that HER in alkaline conditions proceeds via three steps mechanism [11]:

$$M + H_2O + e^- \leftrightarrow MH_{ads} + OH^- \text{ Volmer reaction} \quad (1)$$

$$MH_{ads} + H_2O + e^- \leftrightarrow H_2 + M + OH^- \text{ Heyrovsky reaction} \quad (2)$$

$$MH_{ads} + MH_{ads} \leftrightarrow H_2 + M \text{ Tafel reaction} \quad (3)$$

HER starts with proton discharge by electro-sorption step (Volmer reaction), while further reaction proceeds by electronic-desorption step (Heyrovsky reaction) and/or catalytic-recombination step (Tafel reaction). Thus, the overall reaction progresses via two possible reaction pathways, Volmer-Heyrovsky and Volmer-Tafel. In order to determine the reaction mechanisms, the polarization curves were linearized in accordance with the Tafel equation:

$$\eta = a + b \log|i| \quad (4)$$

where η is the overpotential (V), i is the current density (A cm^{-2}), a and b are the constants of Tafel. While the slope b in the previous equation provides information on the electrochemical mechanism, constant a describes the electrocatalytic activity of the electrode surface [12,35]. Kinetic parameters of HER calculated from Tafel curves recorded in 1 M NaOH solution at different current densities are shown in Table 2.
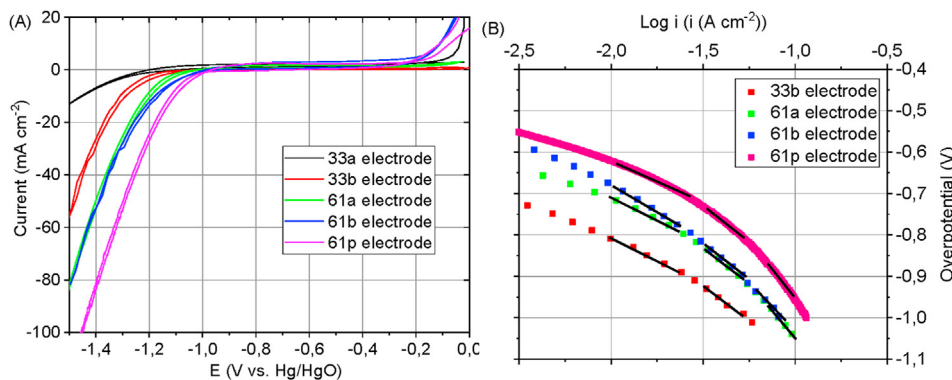

Fig. 7 — The influence of Al content in SHS products (type 3 electrode) before and after etching on the HER polarization curves (A). Tafel plots of the HER (Fig. 6A) occurring on the electrodes (B).

Table 2 – Kinetic parameters of the HER calculated from voltammograms recorded in 1 M NaOH solution at 293 K.

Electrodes	Initial composition in SHS synthesis, Ni:Ti:Al:C	a parameter (V)		Tafel slope, b (V dec⁻¹)		The exchange current density, i_0 (A cm⁻²)		Transfer coefficient, α	
		10-30 mA cm⁻²	115–150 mA cm⁻²	10-30 mA cm⁻²	115-150 mA cm⁻²	10-30 mA cm⁻²	115–150 mA cm⁻²	10-30 mA cm⁻²	115–150 mA cm⁻²
33b electrode	0:2:1.5:1	−1.27		−0.235		3.93×10^{-6}		0.246	
61a electrode	0:2:3:1	−1.17		−0.231		8.72×10^{-6}		0.251	
61b electrode	0:2:3:1	−1.24		−0.283		4.18×10^{-5}		0.205	
61p electrode	0:2:3:1	−1.09	−1.65	−0.242	−0.69	3.17×10^{-5}	4.1×10^{-3}	0.239	0.084
Ni electrode	−//−	−0.786	−1.78	−0.156	−0.951	9.31×10^{-6}	1.35×10^{-2}	0.371	0.060
60a electrode	1:2:3:1	−1.07	−1.52	−0.228	−0.580	2.15×10^{-5}	2.33×10^{-3}	0.254	0.100
60s electrode	1:2:3:1	−1,09	−1,55	−0.337	−0.766	5.71×10^{-4}	9.41×10^{-3}	0.172	0.076

Addition of Ni (14% mol.) to the initial reaction mixture (sample 60a electrode), allows further shift of HER polarization curve towards more positive electrode potentials, indicating an improvement in the electrocatalytic performance (Fig. 8A) compared to sample without Ni (61a electrode). This behaviour is promoted by the formation of catalytically active Ni–Al alloys [33]. The advantage of this approach (preparation of sample 60a) is the possibility of simultaneous etching of Al from several phases (Ni–Al alloys and $Ti_3C_2Al_z$ phase, z > 1) using 10M NaOH solution without the use of HF acid that dissolves both Al and Ni.

Etching and dealloying parameters such as temperature and time have a significant effect on the catalytic activity of resulted material. Etching of the samples without nickel (61t electrode) was carried out at room temperature (at 20 °C) for 2 days and led to a slight increase in the catalytic activity. Therefore, etching of 61p electrode was performed at 70 °C for 2 days that led to a moderate increase in HER activity (Fig. 7A).

Etching of the electrodes containing nickel at 20 °C (60t electrode) or at 70 °C (60p electrode, Fig. S3C) during 2 days leads to only a slight increase of the catalytic activity, probably due to slow etching process. Also, after etching of the Ni-containing sample at a relatively high temperature (160 °C during 2 days, 60n electrode), the electrode loses a significant amount of Al and becomes more porous. At the same time, the HER polarization curve (60n electrode, Fig. S3D) resembles the behaviour of pure nickel electrode, likely due to the changes (probably, oxidation of the surface and Ti–O bonds formation [15]) taking place in MXene catalytically active sites. Therefore, further attention was focused on tuning the etching reaction time. As known, the etching process in MXenes is kinetically controlled [36] and each material requires an individual selection of etching and formation conditions. Sample with increased catalytic activity toward HER was obtained after partial etching in 10M NaOH solution at 70 °C during 5 days (60s electrode, Fig. 8A). Such a relatively long time is probably required due to slower etching of the Ni–Al alloys when compared to pure Al. Thus, these conditions allow to forming MXene/nano-Ni composite layer on the surface of SHS products, which is reflected in an additional decrease in overpotential, when compared to the sample without etching (60a electrode, Fig. 8A). Also, as in case of samples without nickel, further increase of Al content in such materials (60x and 63a electrodes, Table 1) makes it possible to reduce the etching temperature and time, but such electrodes are subject to rapid destruction.

The numbers 1, 2 and 3 (Fig. 8A) denote the regions that correspond to different electrode processes at the Ni surface [37]. After the etching, an increase and broadening of the region (2) is observed, related to the oxidation of metallic Ni to NiO_x; α-$Ni(OH)_2$ was also observed in the samples with Ni. The currents corresponding to this region are higher compared to the metallic Ni electrode, likely due to the formation of nanostructured Ni and the consequent increase of the electrochemically-active surface area.

Another interesting observation is that the HER polarization curves of the 60s electrode sample and Ni electrode (Fig. 8A) are close at low current densities (10−30 mA cm⁻²), but further increase of the current density up to (150−200 mA cm⁻²) leads to lowering HER overpotential by
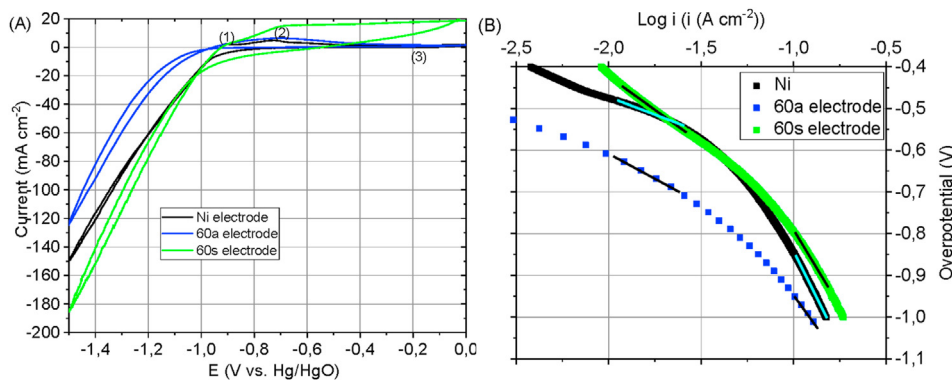
Fig. 8 — The influence of Ni content in SHS products, before and after etching in 10M NaOH on the HER polarization curves (A). Tafel plots of the HER (Fig. 7A) occurring on the electrodes (B).

10 mV for 60s electrode as compared to Ni electrode. The latter indicates that such composites may be promising for boosting HER at relatively high current densities, required for producing reasonable amounts of hydrogen.

The values of Tafel slope for reactions 1, 2 and 3 in case of rate-determining stage (RDS) usually approximately equal of -0.12 V dec^{-1}, -0.04 V dec^{-1}, and -0.03 V dec^{-1}, respectively, but a more detailed analysis of the polarization curves shows the existence of two slopes: at lower potentials and at higher potentials [38]. According to the results of the Tafel analysis, the rate determining step (RDS) at low overpotential is the Heyrovsky reaction, which is related to the electro-desorption step. At higher overpotential, the Volmer reaction is the RDS, where the charge transfer process determines the HER kinetics. As it can be seen (Figs. 7B and 8B, Table 2), the values of Tafel slope for all samples are higher than for pure Ni electrode at lower potentials (current densities). However, at higher potentials (current densities) the values of the Tafel slope become lower than for pure Ni electrode in the case of 60s electrode ($Ti_3C_2(OH)_x$ MXene/nano-Ni composite) and even lower for 60a electrode (SHS products without etching). The comparison of the calculated values of exchange current densities given in Table 2 demonstrate that the electrodes etched in 10M NaOH, both Ni-free and Ni-containing samples, demonstrate better catalytic activity (the exchange current density increases several times). This can be attributed to the formation of $Ti_3C_2(OH)_x$ MXene and to the presence of nanostructured Ni with expectedly higher catalytic activity in the electrochemical reactions. However, at higher potentials, the Ni electrode still shows a higher exchange current density. Therefore, one of the main reasons responsible for the improved catalytic activity of $Ti_3C_2T_x$ MXene/nano-Ni composite at higher potentials is probably the acceleration the Volmer stage in HER process by enhancing the water adsorption and dissociation on the catalyst surface [11,13,39].

One should also take into account that the nanostructuring promotes an increased real surface area available to an electrochemical process. Therefore, CV curves in the short potential range were recorded to estimate the ECSA for several tested electrodes (Fig. 9A, B, C, D). Even after etching, the electrodes with higher Al content show higher OCP values indicating that the etching process continues in 1M NaOH solution. Nonlinear dependence of the current density and

slope on the scan rate for all samples is observed (Fig. 9E), while in the literature for the MXene-based electrodes obtained by HF acid etching and subsequent delamination a linear behaviour was demonstrated [8,40]. Such nonlinear dependence is probably associated with the limitations of ions diffusion between the MXene layers in the mentioned samples (Fig. 9E) for which the MXene formation was not followed by the delamination. Therefore, the ECSA values were estimated from the slop in two ranges 10–60 mVs^{-1} and 60–120 mVs^{-1} and those values are summarised in Table 1. The obtained results are comparable with those mentioned in the literature [8,40].

In case of 60s and 60x electrodes containing nanostructured Ni, the implemented capacitance method for the ECSA estimation might be less suitable due to the oxidation and reduction processes associated with Ni, which can make a significant contribution to the pseudocapacitance and therefore to the ECSA values [18]. In general, the values of ECSA for Ni containing electrodes 60s and 60x should be lower than the electrodes without Ni (61p, 62a), since the addition of Ni inhibits the formation of Ti_3AlC_2 phase and increase the content of unreacted C, along with the other undesired phases in the SHS products (Fig. 4).

The sample 62a electrode shows a considerable increase in capacitance at 1 and 5 mVs^{-1} (Fig. 9E), revealing its potential for supercapacitor applications. Estimated from CV curves for the electrode 62a in extended range (from -0.4 to -0.9V), as showed in (Fig. 9F), the areal capacitance values amount to 0.61, 0.52 and 0.45 F cm^{-2} at 1, 5 and 10 mVs^{-1} respectively, being to the ones mentioned in literature [22,41].

The sample with lower Al content 61p electrode (Ti:Al:C = 2:3:1) and short ball milling time (2 h) after etching surprisingly shows ECSA values similar to those estimated for the samples with higher Al content 62a electrode (Ti:Al:C = 2:3.5:1) and longer ball milling time (6 h). As mentioned previously, such behaviour can be at least partially attributed to some amount of carbon trapped in the carbon reach "cores" of the samples milled for a shorter time. Thus, in these samples, the surface part ("shell") is expected to have a higher Al content, where the etching actually occurs.

To obtain general guidelines regarding the relevant mechanisms at the electrode interfaces, the impedance spectra were recorded for 60s and 62a electrodes. The Nyquist
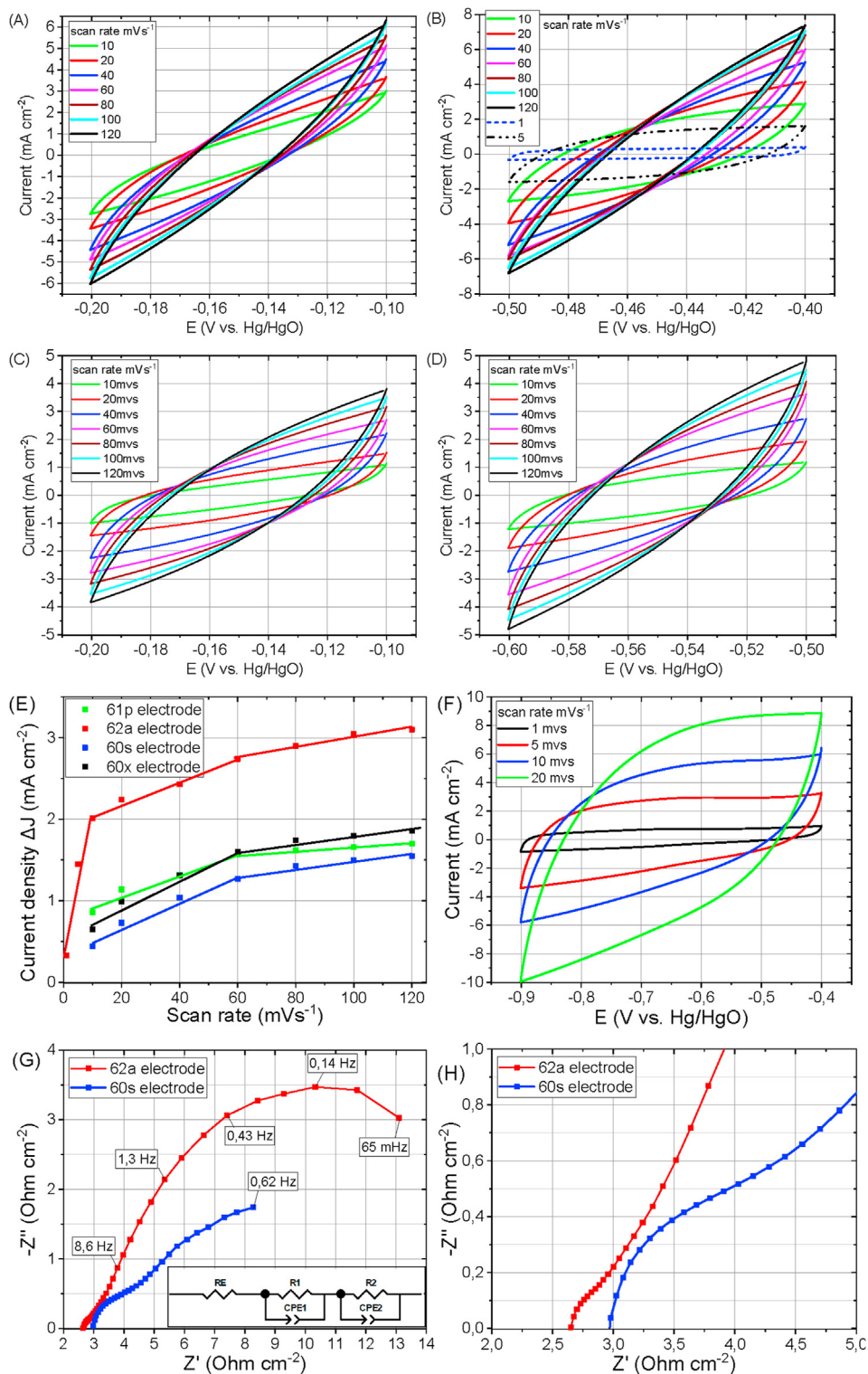
Fig. 9 – CV curves of electrodes 61p (A), 62a (B), and 60s (C), 60x (D) at different scan rates. The differences in current density plots against scan rate for electrodes 61p, 62a, and 60s, 60x (E). CV curves of electrode 62a at different scan rates (F). Electrochemical impedance spectroscopy data and equivalent circuit for electrodes 61p and 60s (G, H).

plots (Fig. 9G and H) showed two resolved semicircles at high and low frequency regions. These data were fitted using the represented equivalent circuit (Fig. 9G).

The "true" capacitance values ($CPE_{(n=1)}$) were calculated from the constant phase elements (CPE) based on the known

equation $C = (R*CPE)^{(1/n)}/R$, with the corresponding values extracted from the fitting data. The fitted impedance spectra are presented in (Fig. S8AB); the fitting parameters are shown in Table 3. In the high-frequency region (around 100 kHz), the intersection of the semicircle with the real axis (Z') is

Table 3 – Metrics of the elements in equivalent circuit as a result of fitting EIS spectra.

Electrodes	R_E ($\Omega.cm^2$)	R1 ($\Omega.cm^2$)	C1 (n = 1) ($\mu F/cm^2$)	n	R2 ($\Omega.cm^2$)	C2 (n = 1) ($\mu F/cm^2$)	N
60s	2.98	0.92	175	0.78	7.62	24,600	0.50
62a	2.66	0.56	1233	0.62	13.27	69,400	0.64

attributed to the overall resistance of the electrode and electrolyte (R_E). The first semicircle at higher frequency (Fig. 9H) is related to the formation of double-layer at the surface of the electrodes, corresponding to the charge transfer resistance (R1) [23,42]. The second semicircle (at lower frequency) is probably related to the pseudocapacitance provided by electrolyte diffusion between the MXene layers [43,44]. In general, the capacitance values for the Ni-free electrodes are higher than for those containing Ni. And for all samples (from EIS and ECSA measurements) the capacitance increases considerably at lower frequencies.

Importantly, the studied electrodes exhibit good electrochemical stability, which, however, depends on the operating conditions (temperature, current density). As an example, the electrode 61p after etching for 2 days at 70 °C in 10M NaOH shows good stability when hydrogen evolution test is performed during 5 cycles from −0.8 to −1.5V, with a scan rate of 1 mVs); no reduction in current was detected. At the same time, a decrease of the current density by 35% is observed after etching the electrode 61p in 10M NaOH for a longer time (8 days at 70 °C), probably due to MXene oxidation. Such behavior, in general, is in line with known limitations towards widespread applications of MXenes in energy storage and conversion applications, including supercapacitors, metal ion batteries and photocatalysis. At the same time, this work intends to show that the proper selection of the material design strategy, including a composite concept, and operation conditions may extend the range of possible scenarios, where these materials can be potentially used.

Conclusions

Performing SHS process in the mixtures with excess of Al (e.g. Ti:Al:C = 2:3:1) allows to introduce additional Al atoms into the MAX phase and to increase the distance between Ti_3C_2 layers in the final SHS products. The composites containing sintered Ni–Al alloys, MAX phase and $Ti_3C_2Al_z$ phase, z > 1 can be obtained using the SHS process of mixtures based on Ni, Ti, Al, C powders with moderate excess of Al (e.g. Ni:Ti:Al:C = 1:2:3:1). The possibility of Al etching from such SHS products in alkaline conditions, followed by the formation of MXenes, was demonstrated and attributed to larger interlayer distance and lower diffusion limitations in the space between Ti_3C_2 layers. Introduction of nickel between Ti_3C_2 layers in such SHS products is probably possible in the form of Ni–Al alloys. Partial alkaline etching of the electrodes prepared directly by SHS of Ni-containing precursors (e.g. Ni:Ti:Al:C = 1:2:3:1) allows the formation of nano-Ni/Ti_3C_2(OH)$_x$ MXene composites with notable electrocatalytic activity. Composite nano-Ni/Ti_3C_2(OH)$_x$ MXene electrodes demonstrate lower HER overpotential at high current densities compared to pure Ni electrode. An enhanced catalytic activity

of nano-Ni/Ti_3C_2(OH)$_x$ MXene composite towards the hydrogen evolution reaction at higher potentials likely can be attributed to the acceleration of the Volmer stage in HER process, by enhancing the water adsorption and dissociation on the catalyst surface.

Declaration of competing interest

The authors declare that they have no known competing financial interests or personal relationships that could have appeared to influence the work reported in this paper.

Acknowledgement

Appendix A. Supplementary data

Supplementary data to this article can be found online at https://doi.org/10.1016/j.ijhydene.2021.01.041.

REFERENCES

[1] Xia Z, Huang Q, Guo S. Recent progress on synthesis, structure and electrocatalytic applications of MXenes. FlatChem 2019. https://doi.org/10.1016/j.flatc.2019.100129.

[2] Li Z, Yu L, Milligan C, Ma T, Zhou L, Cui Y, et al. Two-dimensional transition metal carbides as supports for tuning the chemistry of catalytic nanoparticles. Nat Commun 2018. https://doi.org/10.1038/s41467-018-07502-5.

[3] Gong M, Wang DY, Chen CC, Hwang BJ, Dai H. A mini review on nickel-based electrocatalysts for alkaline hydrogen evolution reaction. Nano Res 2016. https://doi.org/10.1007/s12274-015-0965-x.

[4] Gao G, O'Mullane AP, Du A. 2D MXenes: a new family of promising catalysts for the hydrogen evolution reaction. ACS Catal 2017. https://doi.org/10.1021/acscatal.6b02754.

[5] Quaino P, Juarez F, Santos E, Schmickler W. Volcano plots in hydrogen electrocatalysis-uses and abuses. Beilstein J Nanotechnol 2014. https://doi.org/10.3762/bjnano.5.96.

[6] Eftekhari A. Electrocatalysts for hydrogen evolution reaction. Int J Hydrogen Energy 2017;42:11053–77. https://doi.org/10.1016/j.ijhydene.2017.02.125.

[7] Jin D, Johnson LR, Raman AS, Ming X, Gao Y, Du F, et al. Computational screening of 2D ordered double transition-metal carbides (MXenes) as electrocatalysts for hydrogen evolution reaction. J Phys Chem C 2020. https://doi.org/10.1021/acs.jpcc.0c01460.

[8] Handoko AD, Fredrickson KD, Anasori B, Convey KW, Johnson LR, Gogotsi Y, et al. Tuning the basal plane functionalization of two-dimensional metal carbides (MXenes) to control hydrogen evolution activity. ACS Appl Energy Mater 2018. https://doi.org/10.1021/acsaem.7b00054.

[9] Zeng M, Li Y. Recent advances in heterogeneous electrocatalysts for the hydrogen evolution reaction. J Mater Chem 2015. https://doi.org/10.1039/c5ta02974k.

[10] Seh ZW, Fredrickson KD, Anasori B, Kibsgaard J, Strickler AL, Lukatskaya MR, et al. Two-Dimensional molybdenum carbide (MXene) as an efficient electrocatalyst for hydrogen evolution. ACS Energy Lett 2016. https://doi.org/10.1021/acsenergylett.6b00247.

[11] Mahmood N, Yao Y, Zhang JW, Pan L, Zhang X, Zou JJ. Electrocatalysts for hydrogen evolution in alkaline electrolytes: mechanisms, challenges, and prospective solutions. Adv Sci 2018. https://doi.org/10.1002/advs.201700464.

[12] Protsenko VS, Bogdanov DA, Korniy SA, Kityk AA, Baskevich AS, Danilov FI. Application of a deep eutectic solvent to prepare nanocrystalline Ni and Ni/TiO2 coatings as electrocatalysts for the hydrogen evolution reaction. Int J Hydrogen Energy 2019;44:24604–16. https://doi.org/10.1016/j.ijhydene.2019.07.188.

[13] Gouveia JD, Morales-García Á, Viñes F, Illas F, Gomes JRB. MXenes as promising catalysts for water dissociation. Appl Catal B Environ 2020. https://doi.org/10.1016/j.apcatb.2019.118191.

[14] Naguib M, Unocic RR, Armstrong BL, Nanda J. Large-scale delamination of multi-layers transition metal carbides and carbonitrides "mXenes. Dalton Trans 2015. https://doi.org/10.1039/c5dt01247c.

[15] Li T, Yao L, Liu Q, Gu J, Luo R, Li J, et al. Fluorine-free synthesis of high-purity $Ti_3C_2T_x$ (T=OH, O) via alkali treatment. Angew Chem Int Ed 2018. https://doi.org/10.1002/anie.201800887.

[16] Dall'Agnese Y, Lukatskaya MR, Cook KM, Taberna PL, Gogotsi Y, Simon P. High capacitance of surface-modified 2D titanium carbide in acidic electrolyte. Electrochem Commun 2014. https://doi.org/10.1016/j.elecom.2014.09.002.

[17] Monteiro JF, Ivanova YA, Kovalevsky AV, Ivanou DK, Frade JR. Reduction of magnetite to metallic iron in strong alkaline medium. Electrochim Acta 2016. https://doi.org/10.1016/j.electacta.2016.02.058.

[18] Cossar E, Houache MSE, Zhang Z, Baranova EA. Comparison of electrochemical active surface area methods for various nickel nanostructures. J Electroanal Chem 2020. https://doi.org/10.1016/j.jelechem.2020.114246.

[19] Su D, Wang J, Jin H, Gong Y, Li M, Pang Z, Wang Y. From "waste to gold": a one-pot method to synthesize ultrafinely dispersed Fe2O3-based nanoparticles on N-doped carbon for synergistic and efficient water splitting. J Mater Chem A 2015. https://doi.org/10.1039/c5ta02217g.

[20] Yang L, Zheng W, Zhang P, Chen J, Tian WB, Zhang YM, Sun ZM. MXene/CNTs films prepared by electrophoretic deposition for supercapacitor electrodes. J Electroanal Chem 2018. https://doi.org/10.1016/j.jelechem.2018.10.024.

[21] Wang H, Zhang J, Wu Y, Huang H, Jiang Q. Chemically functionalized two-dimensional titanium carbide MXene by in situ grafting-intercalating with diazonium ions to enhance supercapacitive performance. J Phys Chem Solid 2018. https://doi.org/10.1016/j.jpcs.2017.12.039.

[22] Lukatskaya MR, Kota S, Lin Z, Zhao MQ, Shpigel N, Levi MD, Halim J, Taberna PL, Barsoum MW, Simon P, Gogotsi Y. Ultra-high-rate pseudocapacitive energy storage in two-dimensional transition metal carbides. Nat Energy 2017. https://doi.org/10.1038/nenergy.2017.105.

[23] Xia QX, Fu J, Yun JM, Mane RS, Kim KH. High volumetric energy density annealed-MXene-nickel oxide/MXene asymmetric supercapacitor. RSC Adv 2017. https://doi.org/10.1039/c6ra27880a.

[24] Zhou A, Wang CA, Hunag Y. Synthesis and mechanical properties of Ti3AlC2 by spark plasma sintering. J Mater Sci 2003. https://doi.org/10.1023/A:1024777213910.

[25] Zhou A, Wang CA, Ge Z, Wu L. Preparation of Ti_3AlC_2 and Ti_2AlC by self-propagating high-temperature synthesis. J Mater Sci Lett 2001. https://doi.org/10.1023/A:1013147121618.

[26] Mashtalir O, Naguib M, Mochalin VN, Dall'Agnese Y, Heon M, Barsoum MW, et al. Intercalation and delamination of layered carbides and carbonitrides. Nat Commun 2013. https://doi.org/10.1038/ncomms2664.

[27] Halim J, Lukatskaya MR, Cook KM, Lu J, Smith CR, Näslund LÅ, et al. Transparent conductive two-dimensional titanium carbide epitaxial thin films. Chem Mater 2014. https://doi.org/10.1021/cm500641a.

[28] Lipatov A, Lu H, Alhabeb M, Anasori B, Gruverman A, Gogotsi Y, et al. Elastic properties of 2D Ti3C2Tx MXene monolayers and bilayers. Sci Adv 2018. https://doi.org/10.1126/sciadv.aat0491.

[29] Thomas T, Bowen CR. Effect of particle size on the formation of Ti2AlC using combustion synthesis. Ceram Int 2016. https://doi.org/10.1016/j.ceramint.2015.11.088.

[30] Zhu J, Hu L, Zhao P, Lee LYS, Wong KY. Recent advances in electrocatalytic hydrogen evolution using nanoparticles. Chem Rev 2020. https://doi.org/10.1021/acs.chemrev.9b00248.

[31] Panigrahi BB, Gracio JJ, Chu MC, Cho SJ, Reddy NS. Powder synthesis, sintering kinetics, and nickel-activated pressureless sintering of Ti3AlC2. Int J Appl Ceram Technol 2010. https://doi.org/10.1111/j.1744-7402.2010.02572.x.

[32] Qiu HJ, Xu HT, Liu L, Wang Y. Correlation of the structure and applications of dealloyed nanoporous metals in catalysis and energy conversion/storage. Nanoscale 2015. https://doi.org/10.1039/c4nr05778c.

[33] Tanaka S, Hirose N, Tanaki T, Ogata YH. Effect of Ni-Al precursor alloy on the catalytic activity for a Raney-Ni cathode. J Electrochem Soc 2000. https://doi.org/10.1149/1.1393514.

[34] Halim J, Cook KM, Naguib M, Eklund P, Gogotsi Y, Rosen J, Barsoum MW. X-ray photoelectron spectroscopy of select multi-layered transition metal carbides (MXenes). Appl Surf Sci 2016. https://doi.org/10.1016/j.apsusc.2015.11.089.

[35] Shinagawa T, Garcia-Esparza AT, Takanabe K. Insight on Tafel slopes from a microkinetic analysis of aqueous electrocatalysis for energy conversion. Sci Rep 2015. https://doi.org/10.1038/srep13801.

[36] Anasori B, Lukatskaya MR, Gogotsi Y. 2D metal carbides and nitrides (MXenes) for energy storage. Nat Rev Mater 2017. https://doi.org/10.1038/natrevmats.2016.98.

[37] Hall DS, Bock C, MacDougall BR. The electrochemistry of metallic nickel: oxides, hydroxides, hydrides and alkaline hydrogen evolution. J Electrochem Soc 2013. https://doi.org/10.1149/2.026303jes.

[38] Nikolic VM, Maslovara SL, Tasic GS, Brdaric TP, Lausevic PZ, Radak BB, et al. Kinetics of hydrogen evolution reaction in alkaline electrolysis on a Ni cathode in the presence of Ni-Co-Mo based ionic activators. Appl Catal B Environ 2015. https://doi.org/10.1016/j.apcatb.2015.05.012.

[39] Yu M, Wang Z, Liu J, Sun F, Yang P, Qiu J. A hierarchically porous and hydrophilic 3D nickel–iron/MXene electrode for accelerating oxygen and hydrogen evolution at high current densities. Nanomater Energy 2019. https://doi.org/10.1016/j.nanoen.2019.103880.

[40] Kuang P, He M, Zhu B, Yu J, Fan K, Jaroniec M. 0D/2D NiS2/V-MXene composite for electrocatalytic H2 evolution. J Catal 2019. https://doi.org/10.1016/j.jcat.2019.05.019.

[41] Guo M, Geng W-C, Liu C, Gu J, Zhang Z, Tang Y. Ultrahigh areal capacitance of flexible MXene electrodes: electrostatic and steric effects of terminations. Chem Mater 2020. https://doi.org/10.1021/acs.chemmater.0c02026.

[42] Zhu G, He Z, Chen J, Zhao J, Feng X, Ma Y, Fan Q, Wang L, Huang W. Highly conductive three-dimensional MnO2-carbon nanotube-graphene-Ni hybrid foam as a binder-free supercapacitor electrode. Nanoscale 2014. https://doi.org/10.1039/c3nr04495e.

[43] Zang X, Wang J, Qin Y, Wang T, He C, Shao Q, Zhu H, Cao N. Enhancing capacitance performance of Ti3C2Tx MXene as electrode materials of supercapacitor: from controlled preparation to composite structure construction. Nano-Micro Lett 2020. https://doi.org/10.1007/s40820-020-0415-5.

[44] Mathis TS, Kurra N, Wang X, Pinto D, Simon P, Gogotsi Y. Energy storage data reporting in perspective—guidelines for interpreting the performance of electrochemical energy storage systems. Adv Energy Mater 2019. https://doi.org/10.1002/aenm.201902007.